

Propagation dynamics and optical particle manipulation of circular swallowtail autofocusing beams carrying polynomial power-exponent phase vortices

Zhuang Shen(沈庄), Shandong Tong(童善东), Jian Yu(余建), Yuchuan Yang(杨瑀川), Siying Li(李思颖), Huihong Long(隆辉鸿), and Min Zhou(周敏)

Citation: Chin. Phys. B, 2026, 35 (**8**): 084102. DOI: 10.1088/1674-1056/ae12d6
http://cpb.iphy.ac.cn; http://iopscience.iop.org/cpb

What follows is a list of articles you may be interested in

Fusion of fractional vortex pairs and their transition to integer vortex controlled by optical power

Chunzhi Sun(孙春志), Xiangwei Chen(陈向炜), Huizhong Xu, and Guo Liang(梁果)
Chin. Phys. B, 2025, 34 (**5**): 054202. DOI: 10.1088/1674-1056/adb8b9

Modulation of Bessel-like vector vortex beam using the resonant magneto-optical effect in rubidium vapor

Yan Ma(马燕), Xin Yang(杨欣), Hong Chang(常虹), Ming-Tao Cao(曹明涛), Xiao-Fei Zhang(张晓斐), Rui-Fang Dong(董瑞芳), and Shou-Gang Zhang(张首刚)
Chin. Phys. B, 2025, 34 (**2**): 024202. DOI: 10.1088/1674-1056/ad9c43

Optical storage of circular airy beam in atomic vapor

Hong Chang(常虹), Xin Yang(杨欣), Yan Ma(马燕), Xinqi Yang(杨鑫琪), Mingtao Cao(曹明涛), Xiaofei Zhang(张晓斐), Ruifang Dong(董瑞芳), and Shougang Zhang(张首刚)
Chin. Phys. B, 2024, 33 (**8**): 084202. DOI: 10.1088/1674-1056/ad4bbf

Wavelength-interval switchable Brillouin-Raman random fiber laser through Brillouin pump manipulation

Yang Li(李阳), En-Ming Xu(徐恩明), Rui-Jia Chen(陈睿佳), Yu-Gang Shee, and Zu-Xing Zhang(张祖兴)
Chin. Phys. B, 2024, 33 (**7**): 074209. DOI: 10.1088/1674-1056/ad3efb

Electromagnetic field of a relativistic electron vortex beam

Changyong Lei(雷长勇), Guangjiong Dong(董光炯)
Chin. Phys. B, 2020, 29 (**8**): 084102. DOI: 10.1088/1674-1056/ab96a9

Propagation dynamics and optical particle manipulation of circular swallowtail autofocusing beams carrying polynomial power-exponent phase vortices

Zhuang Shen(沈庄)[1], Shandong Tong(童善东)[1], Jian Yu(余建)[1,†], Yuchuan Yang(杨瑀川)[1], Siying Li(李思颖)[1], Huihong Long(隆辉鸿)[1], and Min Zhou(周敏)[2]

[1] *Chongqing Key Laboratory of Photoelectronic Information Sensing and Transmitting Technology, School of Electronic Science and Engineering, Chongqing University of Posts and Telecommunications, Chongqing* 400065, *China*

[2] *Shenzhen Key Laboratory of Ultra-Intense Laser and Advanced Material Technology, Center for Intense Laser Application Technology, and College of Engineering Physics, Shenzhen Technology University, Shenzhen* 518118, *China*

(Received 11 August 2025; revised manuscript received 28 September 2025; accepted manuscript online 14 October 2025)

Circular swallowtail autofocusing beams carrying polynomial power-exponent phase vortices are constructed for the first time, and their propagation dynamics and particle manipulation capabilities are investigated theoretically and experimentally. The synergistic fusion of polynomial power-exponent vortex phase modulation and the intrinsic autofocusing properties of circular swallowtail beams enables precise and ultra-flexible control of light field structures of this type of beam. The intensity profile, Poynting energy flow, autofocusing ability, and self-healing ability under different combinations of beam parameters are investigated and compared in detail, which confirms the diverse characteristics of the light field structure, the adjustable autofocusing ability, and the excellent self-healing ability. Furthermore, numerical simulation and experimental results prove the capabilities of the new type of beam in terms of particle stable capture and directional transport. The research results of this paper have promising extensive application value in interdisciplinary fields such as biological sciences and physical sciences.

Keywords: circular swallowtail beams, polynomial power-exponent phase vortices, autofocusing ability, self-healing ability, particle manipulation

PACS: 41.85.Ct, 42.60.Jf, 37.10.Vz, 42.50.Wk

DOI: 10.1088/1674-1056/ae12d6 **CSTR:** 32038.14.CPB.ae12d6

1. Introduction

Diffraction catastrophe beams, derived from catastrophe theory, have garnered significant research interest in recent years owing to their unique optical characteristics.[1–4] These beams exhibit diverse geometric structures intrinsically linked to optical caustics, which are governed by potential functions dependent on state and control variables.[5,6] When the number of control parameters does not exceed four, only seven stable catastrophe structures exist: fold, cusp, swallowtail, butterfly, elliptical umbilic, hyperbolic umbilic, and parabolic umbilic catastrophes.[3,7] Each catastrophe type imparts distinct optical propagation behaviors and application potentials. For instance, Airy beams — associated with fold caustics — demonstrate remarkably no diffraction, self-acceleration, and self-healing properties.[8] Similarly, Pearcey beams, corresponding to cusp caustics, exhibit propagation invariance, self-focusing, and self-recovery capabilities.[9] Historically, research has predominantly focused on low-order catastrophes such as Airy and Pearcey beams. However, with advancing investigations, recent studies have expanded to explore higher-order catastrophe beams, particularly swallowtail beams, opening new avenues for optical manipulation and applications.[10,11] These different types of diffraction catastrophe beams have found extensive use in optical micromanipulation,[12,13] microfabrication,[14] superresolution imaging,[15] light bullet generation,[16] and the generation of plasmas,[17] underscoring their versatility in photonics and related fields.

Optical vortices, characterized by their helical phase fronts and phase singularity properties, provide infinite-dimensional degrees of freedom for optical field manipulation through their orbital angular momentum (OAM) modes, thereby opening new paradigms for high-dimensional quantum information encoding,[18] spin–orbit coupling effects of photons,[19] and topological photonics research.[20] By combining structured light field modulation techniques, optical vortices demonstrate the potential to surpass the diffraction limit in super-resolution microscopy,[21] optical tweezers,[22] and nanoparticle manipulation,[23] offering revolutionary tools for biomedicine and nanophotonics. In recent years, the introduction of novel optical vortices, particularly those referred to as noncanonical vortices, has significantly expanded the application value and scenarios of traditional vortex beams.[24–26] Polynomial power-exponent vortices (PPEVs),[27] a novel

†Corresponding author. E-mail: yujian@cqupt.edu.cn

© 2026 Chinese Physical Society and IOP Publishing Ltd. All rights, including for text and data mining, AI training, and similar technologies, are reserved.

class of noncanonical vortices recently proposed, break through the topological charge constraints of traditional vortices via polynomial power-exponent vortex phase modulation, offering unprecedented degrees of freedom for multidimensional optical field manipulation while demonstrating revolutionary potential in microscopic particle manipulation.

Optical vortices typically require embedding into a host beam (e.g., Gaussian beam) for propagation. In recent years, research on the combination of optical vortices and catastrophe beams has developed rapidly, greatly expanding the application value of structured light fields.[28,29] In this work, we present an innovative approach by incorporating PPEVs into circular swallowtail beams (CSB), systematically investigating the propagation dynamics characteristics of this novel hybrid structured light field through theory and experiments. Under different combinations of beam parameters, the beam intensity profile, Poynting energy flow, autofocusing ability, and self-healing ability will be investigated in detail. Furthermore, taking polystyrene particles as an example, this paper will also conduct an in-depth study on the effect of this type of hybrid structured light field in the optical manipulation of particles. Due to the multi-parameter control degrees of freedom, diverse structured light fields can be generated, thus endowing them with multi-functional particle manipulation effects and having important application prospects in fields such as biomedicine and materials physics.

2. Theoretical construction and generation system

Embedding the PPEVs into a CSB, the expression of this hybrid structured light field on the source plane can be constructed as

$$U(r,\varphi,z=0)=Sw\left(\frac{r_0-r}{a\omega_0}\right)\exp\left(\mathrm{i}\sum_{n=1}^{m}l_n\varphi^n\right)t(r,\varphi). \quad (1)$$

Here, r_0 is the initial radius, a is the attenuation factor, ω_0 is the waist radius, and the function $Sw(\bullet)$ denotes the swallowtail diffraction integral, which is fundamentally defined as[10]

$$Sw(x,y,z)=\int_{-\infty}^{\infty}\exp\left[\mathrm{i}\left(s^5+Zs^3+Ys^2+Xs\right)\right]\mathrm{d}s. \quad (2)$$

In the context of the circular swallowtail beam (CSB), the control parameters (X, Y, Z) are mapped to the radial coordinate. Specifically, the argument in our implementation $Sw\left(\frac{r_0-r}{a\omega_0}\right)$ corresponds to setting $X=\frac{r_0-r}{a\omega_0}$ and $Y=Z=0$, which characterizes the specific caustic structure of the CSB. The included exponential term represents the phase of the PPEVs, and l_n denotes the polynomial coefficient of the n-th power-exponent vortex term φ^n. The phase distribution under different combinations of polynomial power-exponent vortex terms can be found from Ref. [27]. $t(r,\varphi)$ is the truncation function that ensures the physical realizability of the beam by constraining its total energy to be finite:

$$t(r,\varphi)=\begin{cases}1, & 0\le r\le R,\ 0\le\varphi\le 2\pi,\\ 0, & \text{other},\end{cases} \quad (3)$$

where R denotes the radius of the integration aperture.

Within the framework of the paraxial approximation, the light field E at any propagation distance z can be obtained by the Fresnel diffraction integral[30]

$$U(\rho,\theta,z)=\int_0^{\infty}\int_0^{2\pi}\frac{E(r,\varphi,0)}{\mathrm{i}\lambda z}\exp\left\{\frac{\mathrm{i}k}{2z}\left[r^2+\rho^2-2r\rho\cos(\theta-\varphi)\right]\right\}r\mathrm{d}r\mathrm{d}\varphi, \quad (4)$$

where k is the wave number, λ is the laser wavelength, and (ρ,θ) represent the polar coordinates at the observation plane. It is very difficult to obtain the analytical solution of Eq. (3). Fortunately, we can obtain its numerical solution based on the matrix multiplication method,[27] thus the propagation dynamics of the hybrid structured beam can be obtained based on numerical simulation. In the subsequent simulations and experiments, we set the beam parameters to $\lambda=671$ nm, $a=0.1$, $\omega_0=0.42$ mm, $r_0=1$ mm, and $R=1.6$ mm.

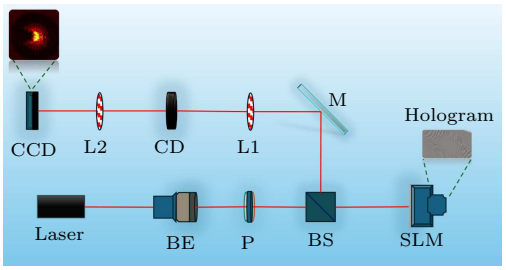


Fig. 1. Experimental generation system for the hybrid structured light field.

Figure 1 shows a schematic diagram of the experimental setup for generating a CSB carrying PPEVs. A Gaussian beam emitted from the laser with a wavelength of 671 nm passes through a continuously adjustable attenuator. The attenuated beam passes through a beam expander (BE) and a linear polarizer (P) to obtain an expanded and collimated linearly polarized beam. Then, the polarized beam transmits through the beam splitter (BS) and is incident on the liquid crystal spatial light modulator (SLM) (1920×1080 array, pixel size 4.5×4.5 μm). Here, the SLM is loaded with a computational hologram obtained based on the complex amplitude modulation method for generating the CSB carrying PPEVs.[31] The beam modulated by the SLM is reflected by the BS and enters a $4f$ system consisting of two lenses (L1 and L2) and a circular diaphragm (CD). The CD can be used to select the positive first-order diffractive light because a blazed grating phase is

added into the hologram. The intensity distribution of the target beam at different propagation distances can be observed by changing the position of the charge-coupled device (CCD).

3. Propagation dynamics characteristics

3.1. Extraordinary autofocusing characteristics

This section studies the autofocusing propagation dynamics characteristics of a CSB carrying PPEVs through simulation and experiments. For convenience, only the case of a CSB carrying a monomial power-exponent vortex term is presented here. Figure 2(a) shows the simulation results of light field propagation when the CSB is carrying traditional canonical vortices ($l_1 = 3$, $n = 1$). It can be found that, while maintaining the autofocusing characteristics, the intensity distribution of this beam presents a typical donut profile structure. However, as shown in Figs. 2(b)–2(f), when the CSB carries PPEVs with different polynomial coefficients, although the autofocusing characteristics are maintained, its light field structure exhibits diversity, and the multi-loop structure on the source plane evolves into various unique intensity profile distributions during propagation. To comprehensively characterize the transverse light field distribution, a systematic numerical simulation and experimental verification were carried out on the light field distribution at different propagation distances, and the corresponding results are shown in Fig. 3. Through comparison, it can be found that the experimental results on the right are in good agreement with the simulation results on the left (see Ref. [27]). In fact, one can clearly see that the phase of the beam with a first-order vortex term shows a smooth spiral phase gradient change, and the energy distribution forms a uniform bright ring, while the spiral phase gradient change of second-order and higher-order vortices is more rapid with the azimuthal angle, and the corresponding phase gradient changes are more complex, causing the energy ring to split into multiple bright rings or other structures.

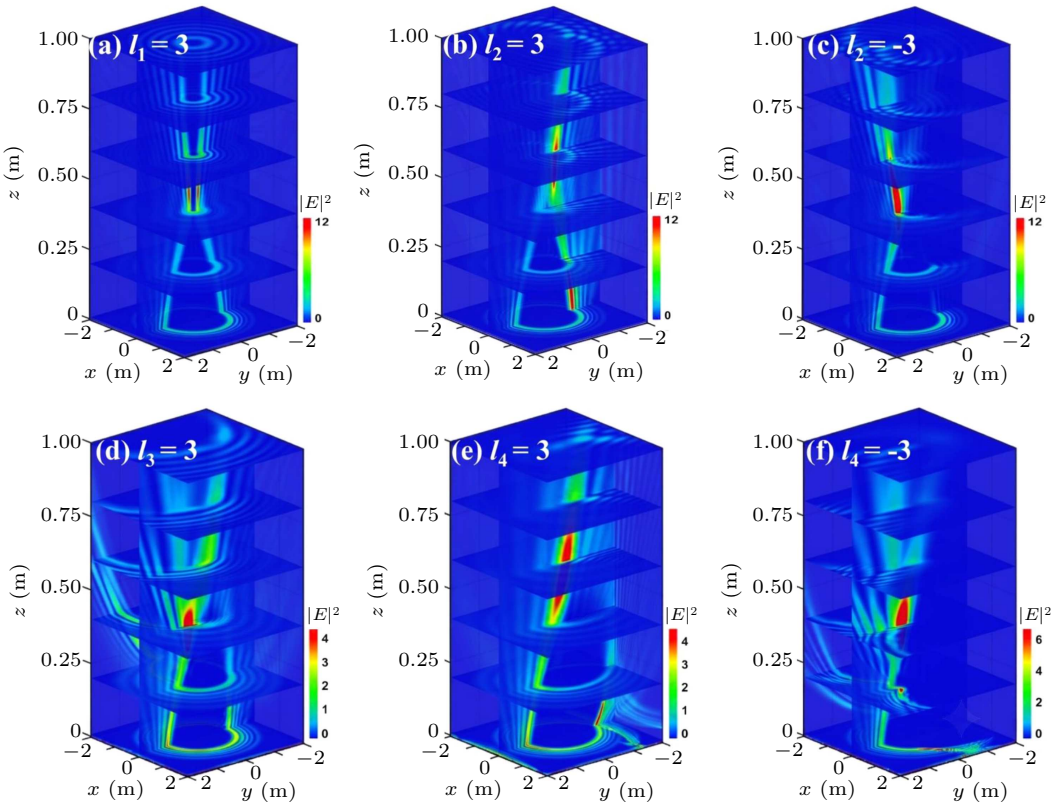


Fig. 2. Simulated autofocusing propagation characteristics of the CSB carrying PPEVs. (a) 3φ; (b) $3\varphi^2$; (c) $-3\varphi^2$; (d) $3\varphi^3$; (e) $3\varphi^4$; (f) $-3\varphi^4$.

To further characterize the influence of different monomial coefficients on the autofocusing properties, Fig. 4 presents the simulation and experimental results of the intensity distribution of the CSB carrying PPEVs at the propagation distance $z = 560$ mm with different single power-exponent vortex terms ($l_1\varphi$, $l_2\varphi^2$, $l_3\varphi^3$, $l_4\varphi^4$), where the coefficient values for each case have been noted in each subgraph. Figures 4(a1)–4(a6) only show the intensity distribution when l_1 and l_3 are positive, and this is because when they are negative, the intensity distribution only exhibits mirror symmetry. In sharp contrast, for power-exponent vortex terms containing $l_2\varphi^2$ and $l_4\varphi^4$, the signs of l_2 and l_4 have a decisive influence on the intensity distribution, as shown in Figs. 4(b)–4(b6) and (c1)–4(c6). Their positive or negative signs directly result in two completely different structural characteristics of the intensity distribution.

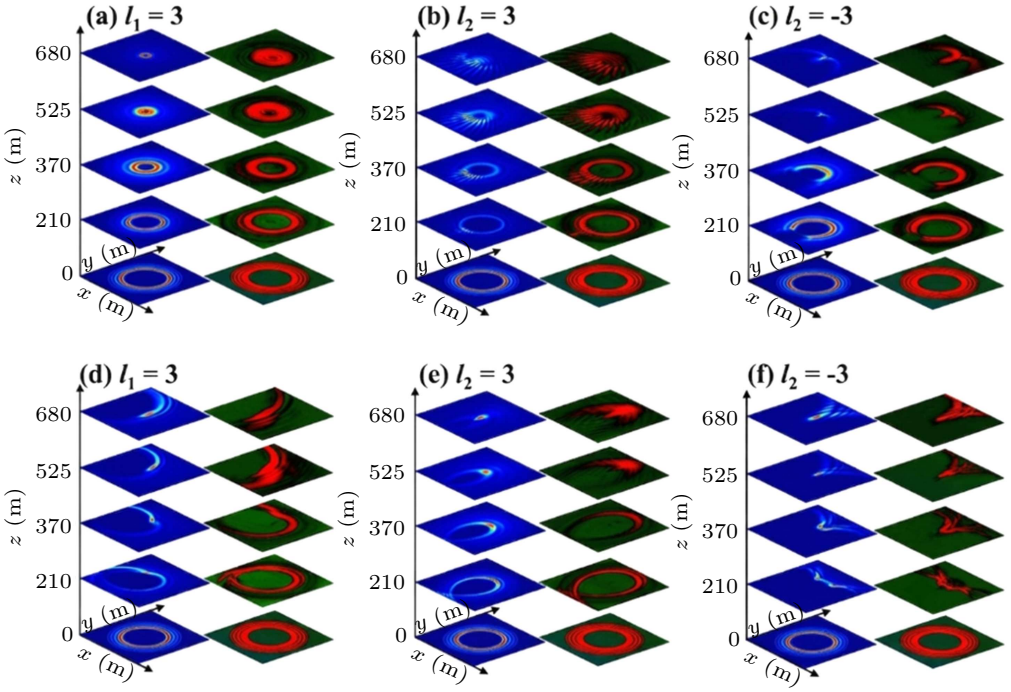


Fig. 3. Intensity distribution simulation and experimental results of the propagation field of the CSB carrying PPEVs. (a) 3φ; (b) $3\varphi^2$; (c) $-3\varphi^2$; (d) 3φ; (e) $3\varphi^2$; (f) $-3\varphi^2$.

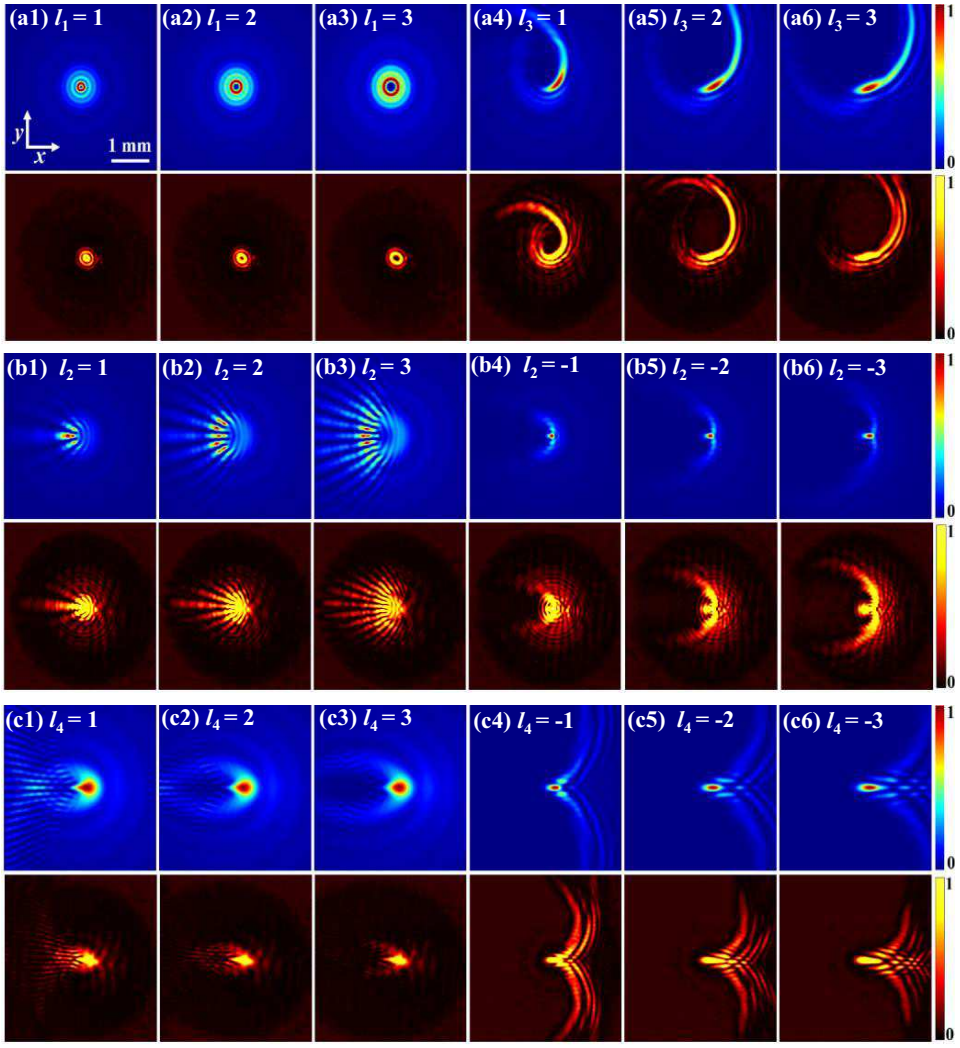


Fig. 4. Simulation and experimental results of the intensity distribution of the CSB carrying only single power-exponent vortex terms ($l_1\varphi$, $l_2\varphi^2$, $l_3\varphi^3$, $l_4\varphi^4$) at the propagation distance $z = 560$ mm.

The propagation dynamics under different combinations of power-exponent vortex terms $l_1\varphi$, $l_2\varphi^2$, and $l_3\varphi^3$ are also investigated. Figure 5 presents the corresponding simulation and experimental results, showing a high degree of agreement between the two. From Figs. 5(a1)–5(c1), it can be observed that under the condition of $l_2 = 1$, when l_1 takes the values ± 1, the beam intensity distribution exhibits an up–down mirror-symmetric characteristic. Notably, as l_1 increases from 1 to 3, the intensity at the original bright spot shifts and converges toward other positions. Figures 5(d1)–5(f1) reveal that under the condition of $l_2 = -1$, the beam intensity distribution displays a tail-like spiral "C-shaped" structure. Furthermore, as the value of l_1 increases, the contour size gradually expands, while the gap in the "C-shape" narrows. Figures 5(a2)–5(c2) reveal another significant phenomenon that when $l_1 = 1$, the sign of l_3 can also induce a mirror-symmetric flipping of the intensity distribution. Notably, under the condition of $l_3 = 1$, as l_1 increases from 1 to 10, the profile of the beam intensity distribution exhibits a pronounced outward expansion trend. By comparing Figs. 5(d2) and 5(e2), it can be clearly observed that there are significant differences in the beam intensity distribution when $l_2 = \pm 3$. Figure 5(f2) shows the beam intensity distribution under the conditions of $l_1 = 10$, $l_2 = 3$, and $l_3 = 1$, whose characteristics fully integrate the unique modulation effects of the three power-exponential vortex terms.

For the combined effect of the high-order power-exponential vortex term $l_4\varphi^4$ and the low-order power-exponential vortex terms ($l_1\varphi$, $l_2\varphi^2$, and $l_3\varphi^3$), we conducted a systematic theoretical analysis and experimental verification of the intensity distribution of the beam at the propagation distance $z = 560$ mm. For $l_4 = 1$, as shown in Figs. 6(a1)–6(f1), the beam exhibits unique spatial distribution characteristics, where the profile head shows a highly concentrated energy, and the overall configuration takes on a typical "sharp-billed bird" shape. When $l_2 = 1$, compared with $l_1 = 1$, the overall profile of the beam slightly expands, and the concentration of energy has decreased. Notably, after introducing the vortex term $l_3\varphi^3$ ($l_3 = 1$), the sharp-billed bird-like structure tilts significantly. With the introduction of more power-exponential vortex terms, the intensity distribution characteristics of the beam show the superposition effect of multiple terms, among which the high-order terms have a particularly significant impact on the intensity distribution. For the case of $l_4 = -1$, as shown in Figs. 6(a2)–6(f2), the intensity distribution presents a "swallowtail"-shaped profile structure. Similarly, when $l_1 = 1$, the beam energy is mainly concentrated in the head area of the swallowtail-shaped structure, while when $l_2 = 1$, the energy distribution significantly spreads to the wings. By comparing Figs. 6(c2) and 6(a2), it can be found that the introduction of the term $l_3\varphi^3$ ($l_3 = 1$) leads to a characteristic tilt of the swallowtail profile. Particularly, with the superposition of more vortex terms, the swallowtail structure shows complex modulated effects, including enhanced non-uniformity of the intensity distribution and the fragmentation of the energy concentration area, among other features. These research findings provide important experimental evidence for a deeper understanding of the physical characteristics and control mechanisms of high-order vortex terms.

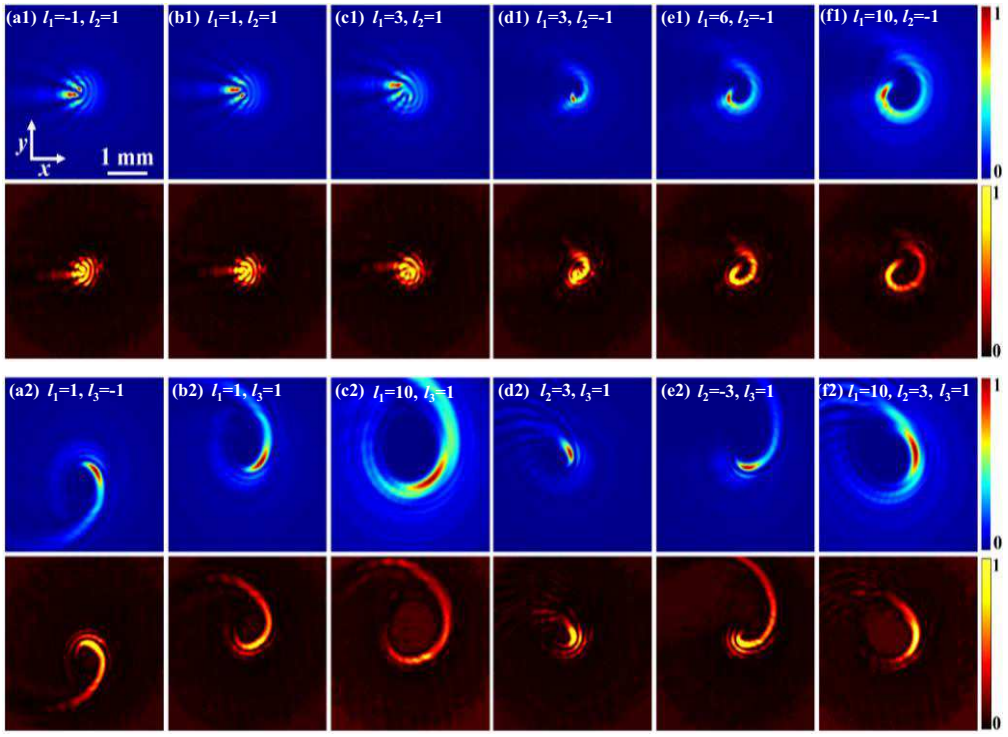


Fig. 5. Simulation and experimental results of the intensity distribution of the CSB carrying different combinations of power-exponent vortex terms $l_1\varphi$, $l_2\varphi^2$ and $l_3\varphi^3$ at the propagation distance $z = 560$ mm.

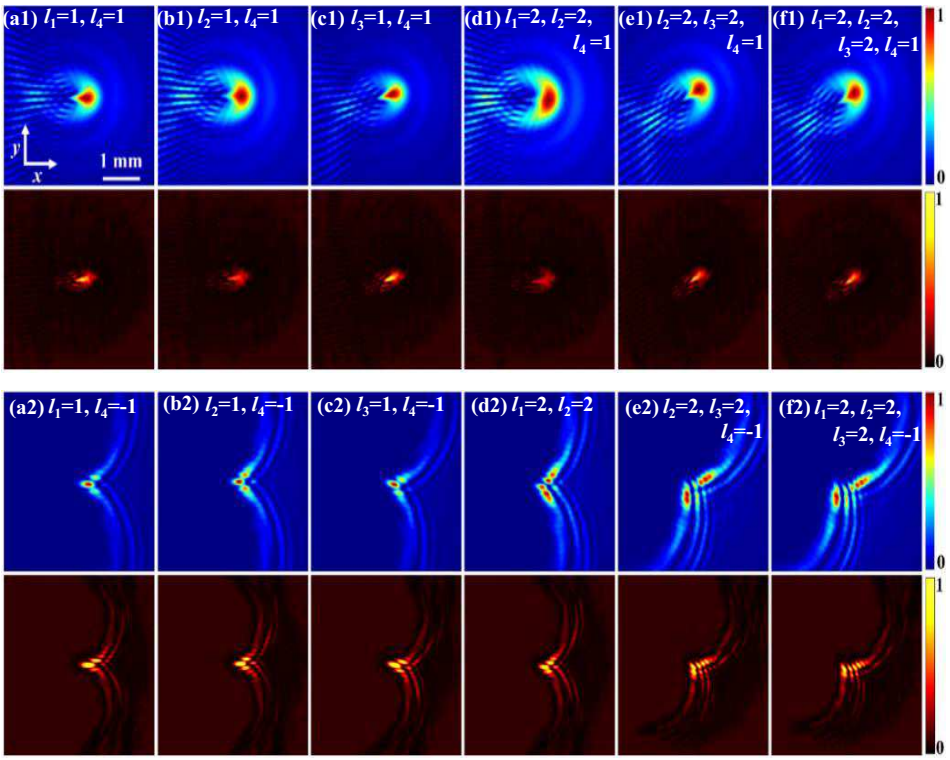


Fig. 6. Simulation and experimental diagrams of intensity distributions for the CSB carrying different combinations of power-exponent vortex terms $l_1\varphi$, $l_2\varphi^2$, and $l_3\varphi^3$, under the conditions of the vortex term $l_4\varphi^4$ ($l_4 = 1$), at the propagation distance $z = 560$ mm.

3.2. Flexible and adjustable autofocusing capability

To quantitatively evaluate the influence of polynomial power-exponential vortices on the autofocusing capability of the beam, the intensity contrast is introduced using the $K = I_{z\mathrm{m}}/I_{0\mathrm{m}}$, where $I_{z\mathrm{m}}$ is the maximum intensity at a plane with a propagation distance z, and $I_{0\mathrm{m}}$ is the maximum light intensity on the initial source plane. By analyzing the K value curves, the autofocusing ability and focusing position of the beam can be obtained.

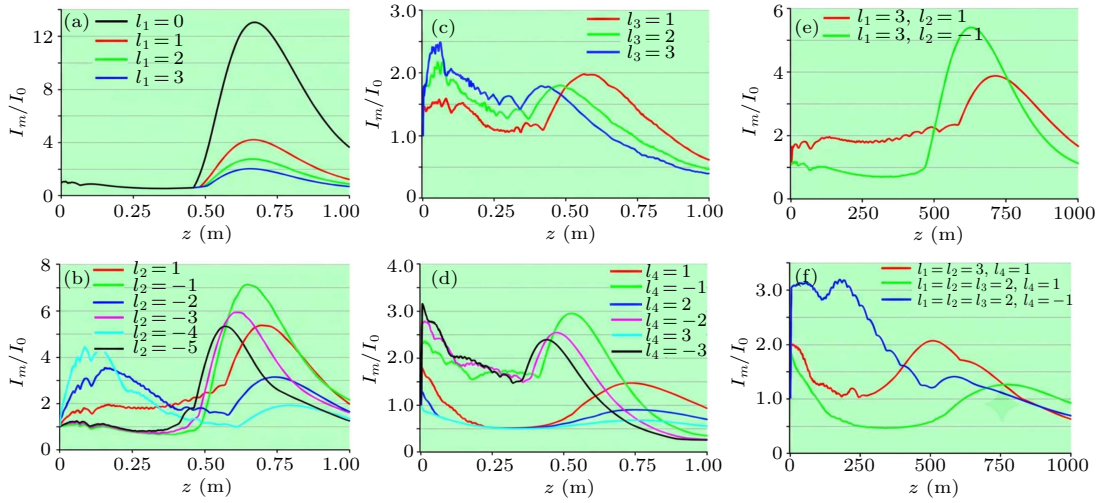


Fig. 7. The K value curves of the CSB carrying different single or multiple power-exponent terms.

Figure 7(a) shows the K value curves of the CSB carrying a single canonical vortex term. It can be seen that, as the topological charge number increases, the autofocusing ability of the beam shows a weakening trend, and the focal length slowly shortens. When the CSB carries the $l_2\varphi^2$ term, the sign of l_2 has a significant impact on the autofocusing ability. As seen from Fig. 7(b), the autofocusing ability when l_2 takes a negative value is significantly stronger than that when the same positive value is taken, and the focal length will also change accordingly. It is worth noting that this rule is also verified in the $l_4\varphi^4$ term, as shown in Fig. 7(d). However, for the $l_3\varphi^3$ term, the positive or negative sign of l_3 affects only the symmetry of the beam intensity distribution and does not change the autofocusing ability. So, Fig. 7(c) only shows the

K value curves when l_3 takes a positive value. By comprehensively comparing Figs. 7(a)–7(d), it can be found that under the modulation effect of the $l_3\varphi^3$ term, the autofocusing ability of the beam is the poorest, and its peak K value is significantly lower than in other cases. In addition, Figs. 7(e)–7(f) show the K value curves of the CSB carrying multiple power-exponent vortex terms. By comparison, it can be found that the overall effect under polynomial modulation is the result of fusing the modulation of each single power-exponent vortex term contained therein. The above results indicate that the CSB carrying PPEVs has a flexible and adjustable autofocusing ability.

3.3. Poynting energy flow and self-healing ability

To fully reveal the propagation dynamics characteristics, this study analyses the transverse Poynting energy flow characteristics of the CSB carrying PPEVs based on numerical simulation. Figures 8(a1)–8(a4) show the transverse Poynting energy flow at different propagation distances ($z = 210$ mm, 370 mm, 530 mm, 680 mm) for the single power-exponent vortex term $l_4\varphi^4$ ($l_4 = -3$). The background in each subgraph represents the light intensity distribution at the corresponding position, and the direction and length of the black arrows, respectively, indicate the energy flow direction and its relative intensity. The results show that during the propagation process, part of the beam energy converges to the head of the swallowtail structure, while the rest of the energy flows to the tail region. Essentially, the Poynting energy flow determines the distribution of the K value curves or autofocusing ability. Figures 8(b1)–8(b4) show the distribution of the Poynting energy flow at the propagation distance $z = 560$ mm when l_4 takes different values ($l_4 = \pm1, \pm2$). It can be found that different l_4 have different Poynting energy flow distributions, but when the positive and negative signs of l_4 are the same, the similarity is relatively high.

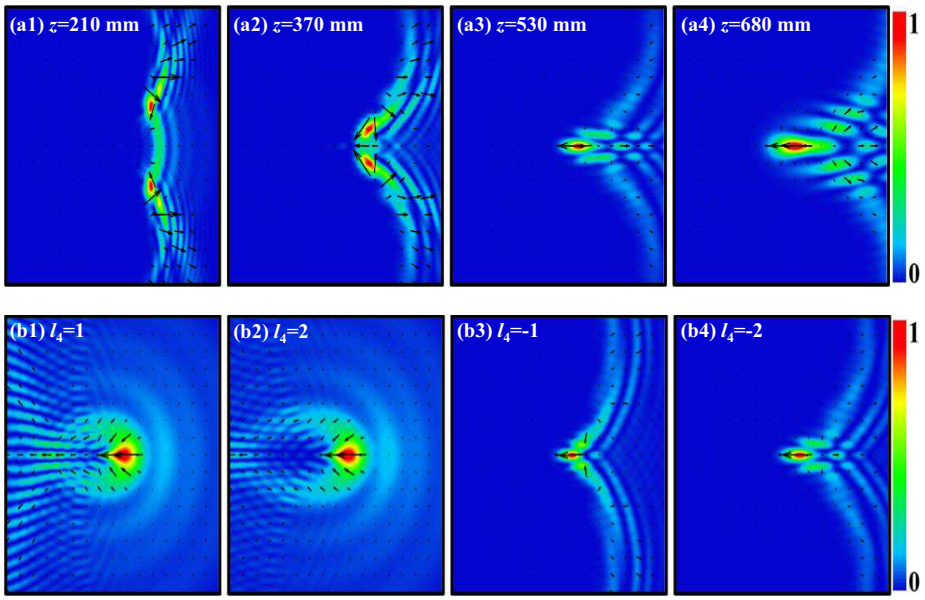


Fig. 8. Transverse Poynting energy flow of the CSB carrying PPEVs.

The self-healing ability of the CSB carrying PPEVs is also investigated through numerical simulation. It is assumed that there exists a fan-shaped obstacle structure with a central angle of $\pi/4$ at the propagation distance $z = 150$ mm. Figure 9 shows the transverse intensity distribution and Poynting energy flow of the CSB carrying PPEVs after being blocked by obstacles under different combinations of power-exponent vortex terms. In particular, Figs. 9(a1)–9(d1), corresponding to the first column, show the original intensity distribution when there are no obstacles, and Figs. 9(a2)–9(d2), corresponding to the second column, show the distributions after being blocked by obstacles. The black arrows represent the Poynting vector, with their direction and length, respectively, characterizing the direction and relative intensity of the energy flow. Figures 9(a1)–9(a6) show the intensity distribution and energy flow characteristics of the CSB without carrying optical vortices. Figures 9(b1)–9(b6) show the intensity distribution and Poynting vector of the CSB carrying a canonical vortex ($l_1 = 3$); Figs. 9(c1)–9(c6) and 9(d1)–9(d6), respectively, show similar simulation results, which correspond to the two types of polynomial power-exponent vortex modulation ($l_1 = 3, l_2 = 1$ and $l_1 = 3, l_2 = -1$). The results show that the main energy of the beam flows to the central area of the beam to achieve beam convergence, while part of the energy flows to the initially blocked area to achieve the self-healing process. That is to say, during the autofocusing propagation process, the beam also demonstrates remarkable self-healing ability. It is worth mentioning that after the autofocusing process is completed the beam will gradually diverge, but the self-healing process still continues.

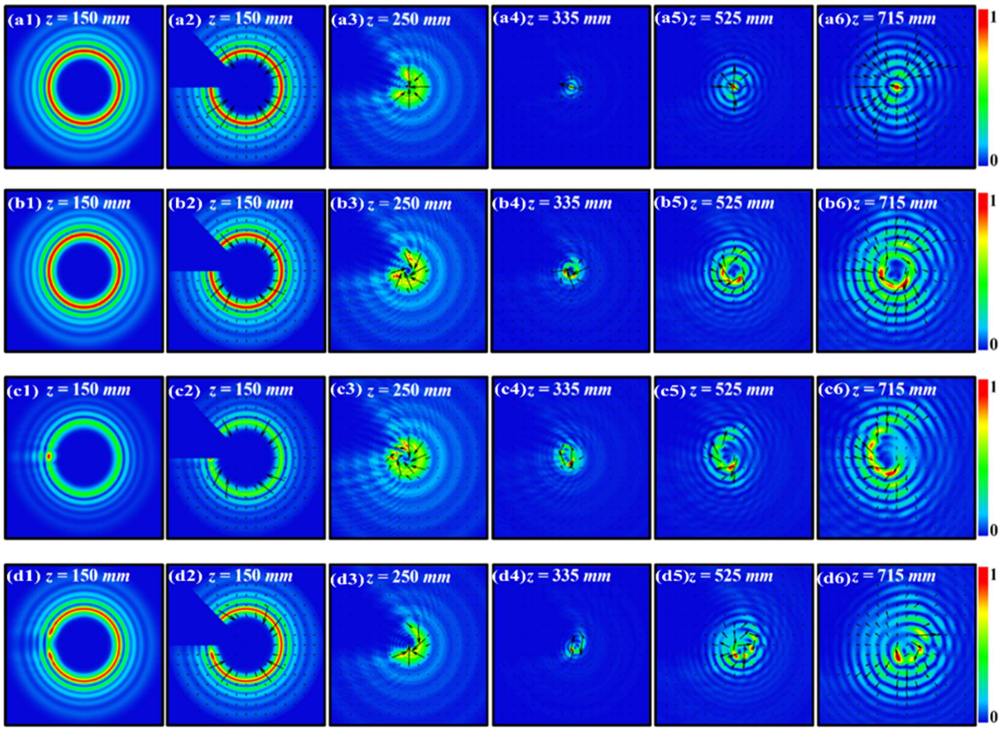


Fig. 9. Transverse intensity distributions and Poynting vectors of the CSB carry different polynomial power-exponent vortex terms under blocked conditions at different propagation distances.

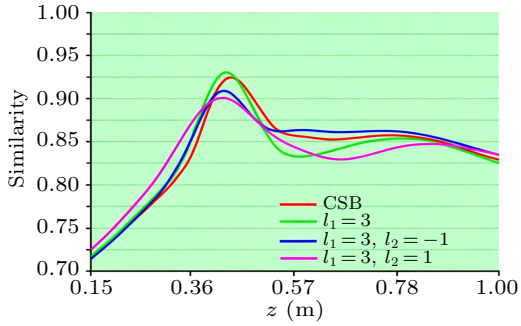


Fig. 10. Similarity curves of the CSB carry different polynomial power exponent vortex terms.

To quantitatively characterize the self-healing ability of the CSB carrying different polynomial power-exponent vortex terms, Fig. 10 presents the similarity curves, which can be calculated according to Ref. [32]. It can be seen from the trend of the curve change that after being blocked at $z = 150$ mm, with increase of the propagation distance, the similarity value continues to rise and reaches the maximum value near the focal plane. However, as the transmission distance further increases, the similarity values all decrease to a certain extent, indicating that the self-healing effect gradually weakens. The similarity data show that the beam always maintains good self-healing characteristics, and the polynomial coefficients can regulate the self-healing effect to a certain extent.

4. Particle manipulation application

Capitalizing on the multi-parameter modulation capability, the CSB carrying PPEVs can generate light fields with diverse novel structures, thereby enabling the formation of versatile optomechanical potential wells. This opens up possibilities for achieving diverse capture and manipulation effects of particles. Based on the experimental system shown in Fig. 1, we further established a holographic optical tweezers experimental system for particle capture and manipulation, as shown in Fig. 11. After the beam is generated at the back focal plane of lens 2, it is reflected by a dichroic mirror and directed into a high numerical aperture objective (100×, NA = 0.80), which focuses the beam onto a sample-loaded glass slide. Meanwhile, yellow illumination light passes through the sample, objective, dichroic mirror (DM), reflective mirror (RM), optical filter (OF), and lens (L). Ultimately, the polystyrene microspheres captured or manipulated by the light field are observed by the CCD camera.

Figure 12 presents experimental results of particle trapping and manipulation under several CSBs carrying PPEVs. The simulated intensity patterns are shown in sequence in Figs. 12(a1)–12(d1), and the experimentally captured beam profiles are also presented in the lower left corner of each subgraph. It can be seen that the light intensity profiles obtained from the simulation and the experiment are basically consistent. To better visualize the guiding and trapping effects on microspheres, the intensity profiles of the target beams are extracted and superimposed on the corresponding trapping sequence subgraphs, clearly presenting the motion trajectory of polystyrene microspheres. Figures 12(a2)–12(a5) show the experimental results of the beam successively capturing three polystyrene microspheres when $l_2 = 1$. It can be seen that the

positions where the microspheres are stably captured are consistent with the gradient force distribution of the optical trap. Figures 12(b2)–12(b5) and 12(c2)–12(c5), respectively, show the movement trajectories of the polystyrene microspheres guided by the beam with parameters ($l_3 = 1$) and ($l_2 = -3$, $l_3 = 1$). By recording the movement time of the microspheres, the results show that under the conditions of ($l_2 = -3$, $l_3 = 1$), the speed at which the beam guides and captures the microspheres is significantly faster than that under the parameter ($l_3 = 1$). This speed difference can be explained by the distinction in the OAM density distribution of the beam.[33] Figures 12(d2)–12(d5) show the movement trajectory of microspheres guided and captured by a swallowtail-shaped beam. It can be seen that the microspheres, which are originally not in the same imaging layer as the beam, are gradually guided from the tail fin to the head of the swallowtail-shaped profile beam under the attraction of the beam gradient force, and gradually move into the same imaging layer as the beam spot, and are finally confined to the maximum light intensity position (maximum gradient force trap).

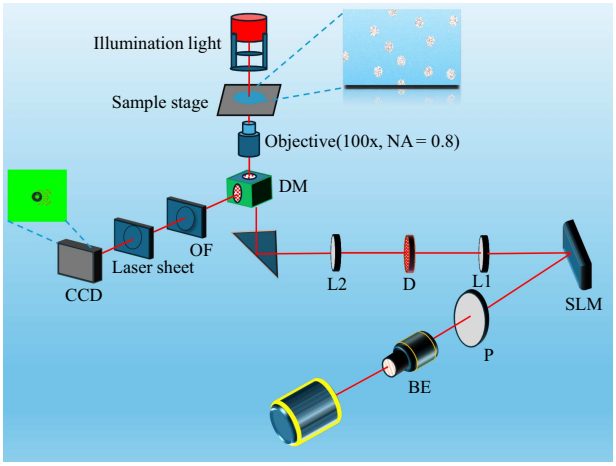


Fig. 11. Experimental setup of the holographic optical tweezers system.

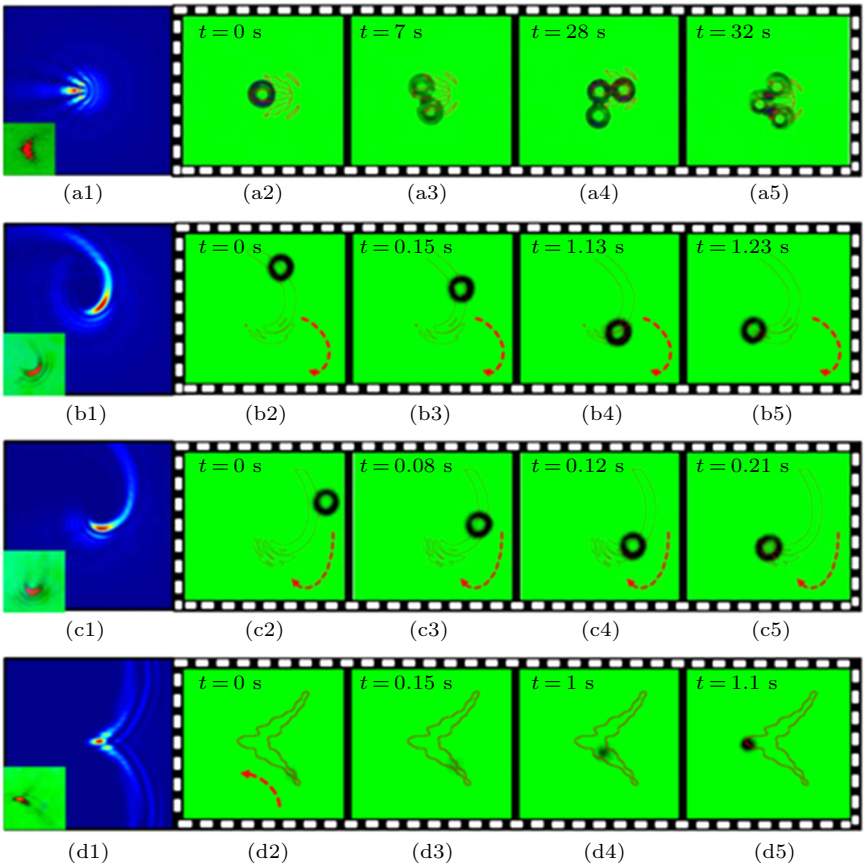


Fig. 12. Experimental results of beam guidance and capture of polystyrene microspheres under different beam parameters.

5. Conclusion and perspectives

The combination of catastrophe beams and optical vortices has been a hot topic in the research area of novel structured light fields in recent years, greatly enriching the theoretical basis of light field manipulation and expanding the application value of structured light fields in particle manipulation, free-space optical communication, and optical imaging. This study systematically investigated the propagation dynamics of CSBs integrated with PPEVs. Distinct from previous research,[27] the structured optical field constructed herein not only retains the autofocusing capabilities of CSBs but also incorporates the multi-parameter tunability characteristic of PPEVs. Through combinatorial modulation of beam parameters, flexible control over intensity profiles, autofocusing

performance (K value), and self-healing properties has been achieved. Utilizing a self-built optical tweezers system, we have experimentally demonstrated the beam's advanced application capabilities in multi-particle manipulation and directional particle transport, which have promising extensive application value in interdisciplinary fields such as biological sciences and physical sciences.

Acknowledgements

This work is supported by the National Natural Science Foundation of China (Grant No. 62105049), the Natural Science Foundation of Chongqing (Grant No. cstc2021jcyj-msxmX1119), the Science and Technology Research Project of Chongqing Education Commission (Grant No. KJQN202100618), the Chongqing Postdoctoral Research Fund Project (Grant No. D63012022051), the Doctoral program sponsored by Chongqing University of Posts and Telecommunications (Grant No. E011A2022310), and the Natural Science Foundation of Top Talent of SZTU (Grant No. GDRC202313).

References

[1] Ren Z J, Ying C F, Jin H Z and Chen B 2015 *J. Opt.* **17** 105608
[2] Teng H A, Qian Y, Lan Y P and Cui W T 2021 *Opt. Express* **29** 3786
[3] Zannotti A, Diebel F, Boguslawski M and Denz C 2017 *New J. Phys.* **19** 053004
[4] Teng H A, Hu J T, Cai Y M, Lan Y P and Qian Y X 2022 *Res. Phys.* **42** 105991
[5] Berry M V and Upstill C 1980 *Prog. Opt.* **18** 257
[6] Kravtsov Y A, Orlov Y I 2012 *Caustics, Catastrophes and Wave Fields* [M]. Berlin Heidelberg: Springer Science & Business Media
[7] Zeeman E C 1976 *Catastrophe theory* **234** 65
[8] Efremidis N K, Chen Z, Segev M and Christodoulides D N 2019 *Optica* **6** 686
[9] Wang Y H 2021 *J. Opt. Soc. Am. A* **38** 1726
[10] Teng H A, Qian Y X, Lan Y and Cui W T 2021 *Opt. Lett.* **46** 270
[11] Sun Z, Hu J T, Wang Y S, Li X Z and Qian Y X 2024 *Opt. Express* **32** 13266
[12] Baumgartl J, Mazilu M, Dholakia K 2008 *Nat. Photon.* **2** 675
[13] Yang Y Z, Wu Y, Zheng X Q, Shi J Y, Luo Y J, Huang J H and Deng D G 2023 *Opt. Lett.* **48** 3535
[14] Courvoisier F, Stoian R, Couairon A 2016 *Opt. Laser Technol.* **80** 125
[15] Vettenburg T, Dalgarno H I, Nylk J, Coll-Lladó C, Ferrier D E K, Čižmár T, J Gunn-Moore F and Dholakia K 2014 *Nat. Methods* **11** 541
[16] Panagiotopoulos P, Papazoglou D G, Couairon A and Tzortzakis S 2013 *Nat. Commun.* **4** 2622
[17] Li L, Li T, Wang S M and Zhu S N 2011 *Phys. Rev. Lett.* **107** 126804
[18] Kong L J, Sun Y F, Zhang F R, Zhang J F and Zhang X D 2023 *Phys. Rev. Lett.* **130** 053602
[19] Chen J, Yu L, Wan C H and Zhan Q W 2022 *ACS Photon.* **9** 793
[20] Wang H W, Tang G J, He Y, Wang Z, Li X F, Sun L, Zhang Y, Yuan L Q, Dong J W and Su Y K 2022 *Light Sci. Appl.* **11** 292
[21] Zhang B Y, Daly S, Zhu C X, Lenz M O, Weiss L E, Needham L M, Peters R, Lee S F and O'Holleran K 2024 *Optica* **11** 1519
[22] da Fonseca A L, Diniz K, Monteiro P B, et al 2024 *Phys. Rev. Res.* **6** 023226
[23] Vosshage P, Otero C M, Schuknecht F, Huergo M A, Feldmann J and Lohmüller T 2025 *Phys. Chem. C* **129** 8262
[24] Yang Y Q, Dou J T, Xu J Q, Li B and Hu Y Y 2024 *New J. Phys.* **25** 123054
[25] Yu X Y, Fan J Q, Li X, Zhu H F, Nie S P, Ma J and Yuan C J 2025 *Lightw. Technol.* **43** 2535
[26] Shan S X, Xu K J, Liu X W, Yu X Y, Liu M S, Zhang W B, Cheng S B, Zhu D S and Yang W X 2025 *Phys. Lett. A* **555** 130802
[27] Yu J, Tong S D, Long H H, Zhang Z, Zhou M, Li S and Yang Y C 2025 *Opt. Lasers Eng.* **191** 108989
[28] Zang X, Wang F, Dan W S, Zhou Y M and Zhou G Q 2022 *Opt. Laser Technol.* **155** 108398
[29] Rodríguez-Fajardo V, Flores-Cova G, Rosales-Guzmán C and Perez-Garcia B 2024 *J. Phys. Photon.* **6** 045015
[30] Collins S A 1970 *J. Opt. Soc. Am.* **60** 1168
[31] Zhou Y, Li R Z, Yu X H, Yan S H, Li X, Gao W Y, Liu C, Peng T, Yang Y L, Min J W, Wang P, Qu J and Yao B L 2021 *Acta Photon. Sin.* **50** 1123001
[32] Zhang H L, Deng H J, Wang X and Chu X X 2022 *Optik* **251** 168478
[33] Pei Z H, Huang S J, Chen Y and Yan C 2021 *J. Mod. Opt.* **68** 224